JOURNAL OF APPLIED PHYSICS 98, 094303 (2005)

Phonon-assisted ballistic to diffusive crossover in silicon nanowire transistors

M. J. Gilbert,[a] R. Akis, and D. K. Ferry
Department of Electrical Engineering and Center for Solid State Electronics Research, Arizona State University, Tempe, Arizona 85287-5706

(Received 5 July 2005; accepted 20 September 2005; published online 2 November 2005)

As transistors get smaller, the simulations require full quantum-mechanical treatments. Most such approaches have treated the transport as ballistic, ignoring the scattering that is known to occur in such devices. We present the results of a three-dimensional, self-consistent quantum simulation of a silicon nanowire transistor. In these simulations we have included phonon scattering through a real-space self-energy assuming weak interactions. In these silicon nanowire transistors, the ballistic to diffusive crossover occurs at much smaller distances than previously anticipated. © *2005 American Institute of Physics*. [DOI: 10.1063/1.2120890]

I. INTRODUCTION

The metal-oxide-semiconductor field-effect transistor (MOSFET) has been a staple of the semiconductor industry for many years, with progress following a well-known scaling relationship.[1] Nevertheless, it is becoming increasingly clear that the continued scaling of these devices will not meet the expected performance requirements and other solutions are under examination.[2] In the silicon area, many transistor structures, such as finfets[3] and trigate transistors[2] have shown interesting promise. With such device concepts, more scaling is expected, and 15 nm gate lengths are scheduled for production before the end of this decade. Such short gate length devices have been demonstrated by Intel[2] and AMD,[4] and IBM has recently shown a 6 nm gate length *p*-channel transistor.[5] While the creation of these very small transistors is remarkable enough, the fact that they seem to operate in a quite normal fashion is perhaps even more remarkable. Almost 25 years ago, the prospect of making such small transistors was discussed, and a suggested technique for a 25 nm gate length, Schottky source-drain device, was proposed.[6] At that time, it was suggested that the central feature of transport in such small devices would be that the microdynamics could not be treated in isolation from the overall device environment (of a great many similar devices). Rather, it was thought that the transport would by necessity be described by quantum transport and that the array of such small devices on the chip would lead to considerable coherent many-device interactions. While this early suggestion does not seem to have been fulfilled, as witnessed by the quite normal behavior of the above-mentioned devices, there have been many subsequent suggestions for treatment via quantum transport.[7–11] Moreover, there is ample suggestion that the transport will not be normal, but will have significant ballistic transport effects[12] and this, in turn, will lead to quantum transport effects.

Recently, we presented a fully quantum-mechanical, and three-dimensional, ballistic simulation of small silicon quantum-wire MOSFETs.[13] In this approach, the full Poisson equation solution was used to determine the local potential, and a recursive scattering matrix approach was used to determine the transport through the device. In this process, each iteration from one transverse slice of the device to the next, a local Dyson's equation is solved with the slice Hamiltonian. This means that we can modify this Hamiltonian by the direct inclusion of a slice self-energy as well as a self-energy coupling between the slices where that is appropriate. This self-energy term describes the dissipation within the device, and our approach here is to describe just how this term is formulated and handled.

There have been many different approaches to including dissipation in quantum simulations. Statistical approaches introduce random-phase fluctuations into the simulations.[14,15] The major drawback for such an approach is that a large sample space is required over which to average, and this entails a great many runs to have any valuable results. Another method is to add an imaginary term to the Hamiltonian which represents the phase-breaking time of the electron in the system under consideration.[16,17] While this approach seems reasonable for a system that is in equilibrium, it is not clear that it is applicable when the system is driven out of equilibrium. The imaginary term is constant throughout the device, and therefore fails to consider the inhomogeneous density in the out of equilibrium system. This approach has also been questioned as not conserving current,[18] but this fails to properly consider the entire dissipative current.[19] Dissipation may also be included through the use of Büttiker probes.[20,21] While this approach is an improvement over the use of a phase-braking related term, in that it is current conserving, it suffers from the fact that an additional loop must be included to insure that the probes do not change the number of electrons in the system, nor does it account for the spatial inhomogeneity of the density and the scattering. Moreover, a fitting parameter must be used to calibrate the probes to the proper low-field mobility. A relaxation-time approximation has also been used in approaches utilizing either the density matrix[22,23] or the Wigner function.[24]

In most device simulations being utilized today, a recursive technique is used, either for the wave function[13,25] or for

[a]Electronic mail: mgilbert@mail.utexas.edu

 © 2005 American Institute of Physics

Downloaded 09 Jul 2010 to 128.174.190.86. Redistribution subject to AIP license or copyright; see http://jap.aip.org/jap/copyright.jsp

Green's function.[26] On the other hand, phonon scattering in one- and two-dimensional systems (quantum wires and quantum wells, respectively) is usually treated as transitions between transverse modes.[27,28] Emberly and Kirczenow[29] have introduced inelastic scattering in a recursive wave-function approach and Lake and Datta have done so for the nonequilibrium Green's function.[30] But these approaches did not make full use of the computation in real space that is the heart of such recursive approaches. More recently, Register and Hess[31] have also introduced inelastic processes for the wave function, in a complicated computational scheme.

In this paper, we present the above-mentioned method for including separable scattering mechanisms in a site-representation self-energy. This approach can be used in any numerical technique based on a propagating Hamiltonian, such as the recursive wave function or Green's functions, without violating current continuity and without using fitting parameters. In the next section, we review the use of a self-energy term in the Hamiltonian and point out the conversions that are necessary for the computation. We then derive the contributions for acoustic deformation potential scattering and intervalley scattering with both *f*- and *g*-type processes. This model is then used with large cross-section devices ("bulk" devices) to evaluate the mobility at several different doping densities. Finally, we apply this method to a silicon-on-insulator (SOI) quantum wire, trigate MOSFET to determine the channel length at which the ballistic motion is taken over by normal diffusive (mobility-dominated) transport.

II. THE SELF-ENERGY TERM

The details of the computational scheme which we employ were described previously in Ref. 13. The heart of the recursion arises from Eqs. (19)–(22) of that paper. The wave function is represented by the excitation matrix C_j^i, where $j=1,2$ for propagation directions and i is the slice index. If we take the channel direction as x, and the transverse directions as y and z, then for N grid points in the y direction and M grid points in the z direction, the dimension of each C_j^i is $NM \times NM$. The recursion is obtained from one slice to the next via Eqs. (21) and (22) as

$$C_2^{i+1} = P_2^i = (H_i - E - H_t^{i,i+1} C_2^i)^{-1} H_t^{i,i+1} \tag{1}$$

and

$$C_1^{i+1} = P_1^i = C_2^{i+1} C_1^i. \tag{2}$$

Here, $H_t^{i,i+1}$ is the hopping Hamiltonian that describes the standard finite-difference coupling from each element of one slice to the corresponding element of the next slice. The quantity H_i is the bare Hamiltonian for the slice itself and contains "diagonal" terms for the on-site terms as well as hopping terms to adjacent sites within the slice. In essence, (1) is a form of the Dyson's equation for iterative solutions of Green's-function type behavior.[32] In fact, the two C parameters are proper Green's functions, but are normalized by the hopping terms to be dimensionless. In our simulation, the wave functions themselves are derived from these parameters. Here, C_2^i plays the role of the one-site Green's function $G(i,i)$, and C_1^i plays the role of the on-site Green's function $G(0,i)$.[26] Hence, the hopping Hamiltonian already plays the role of the hopping self-energy term that couples one slice to the next.

Because of the form of the above two equations, it becomes quite simple to modify the recursive formulation by the addition of an on-site self-energy in which

$$H_0 \equiv H_i \rightarrow H = H_i + \Sigma_i. \tag{3}$$

The self-energy Σ has both real and imaginary parts, with the latter representing the dissipative interactions. In semiconductors, the scattering is weak, and is traditionally treated by the first-order time-dependent perturbation theory, which yields the common Fermi golden rule for scattering rates. With such weak scattering, the real part of the self-energy can generally be ignored for the phonon interactions, and that part that arises from the carrier-carrier interactions is incorporated into the solutions of Poisson's equation by a local-density approximation, which approximately accounts for the Hartree-Fock corrections.[33]

In the many-body formulations of the self-energy, the latter is a two-site function in that it is written as[32]

$$\Sigma(\mathbf{r}_1, \mathbf{r}_2). \tag{4}$$

In our case, where we are using transverse modes in the quantum wire, this may be rewritten as

$$\Sigma(i,j;i',j',x_1,x_2). \tag{5}$$

Here, the scattering accounts for transitions from transverse mode i,j at position x_1 to $i'j'$ at position x_2. Generally, one then makes a center-of-mass transformation[34,35]

$$X = \frac{x_1 + x_2}{2}, \quad \xi = x_1 - x_2, \tag{6}$$

and then Fourier transforms on the difference variable to give

$$\Sigma(i,j;i',j',X,k_x) = \frac{1}{2\pi} \int d\xi e^{i\xi k_x} \Sigma(i,j;i',j',X,\xi). \tag{7}$$

The center-of-mass position X remains in the problem as the mode structure may change as one moves along the channel. At this point, the left-hand side of (7) is the self-energy computed by the normal scattering rates, such as was done in quantum wells and quantum wires previously.[27,28] However, these previous calculation usually used the Fermi golden rule, which is an evaluation of the bare self-energy in (7). In many-body approaches, one normally does not use the energy-conserving delta function that is the central part of the Fermi golden rule. Rather, this function is broadened into the *spectral density*, through the use of the self-consistent Born approximation.[36] In this way, off-shell effects are taken into account through this broadening of the relationship between momentum and energy. In semiconductors, however, we have already noted that the scattering is weak. It has been pointed out that these off-shell corrections are only important in fast processes where we are interested in femtosecond response and their neglect introduces only slight errors for times large compared to the collision duration.[37] Moreover, the broadening of the delta function will not be apparent

Downloaded 09 Jul 2010 to 128.174.190.86. Redistribution subject to AIP license or copyright; see http://jap.aip.org/jap/copyright.jsp

when we reverse the Fourier transform of (7), as the area under the spectral density remains normalized to unity.[32] Since our recursion in (1) and (2) is in the site representation, rather than in a mode representation, we have to reverse the Fourier transform in (7) to get the x-axis variation, and do a mode-to-site unitary transformation to get the self-energy in the form necessary for the recursion. This is the subject of the rest of this section, where we discuss the different phonon processes.

A. Acoustic phonons

In our approach, as in most semiconductor theory, we treat the scattering as weak, as we have already discussed above. Hence, we can use the Fermi golden rule expression, equivalent to a first-order, non-self-consistent Born approximation, for each scattering process and generate a real space self-energy from it. In particular, the imaginary part of the self-energy is related to the scattering rate via

$$\mathrm{Im}\{\Sigma(i,j;i',j',X,k_x)\} = \hbar\left(\frac{1}{\tau}\right)_{i,j}^{i',j'}, \tag{8}$$

and it is the latter scattering rate which we calculate. This result will be a function of the x-directed momentum (which is related, in turn, to the energy of the carrier) in the quantum wire. The Fermi golden rule scattering rate for acoustic phonons is treated in nearly all textbooks, and the only modification is to account for the transverse modes of the quantum wire. As mentioned above, this has previously been treated for quantum wells[27,38] and for silicon quantum wires.[28] Hence, we do not repeat the microscopic details of such a calculation, but begin with the general form

$$\left(\frac{1}{\tau}\right)_{i,j}^{i',j'} = \frac{2\pi}{\hbar}\frac{D_{\mathrm{ac}}^2 k_B T}{2\rho v_s^2} I_{n'm'}^{nm} \sum_{\mathbf{k}'} \delta(E_{k'} - E_k). \tag{9}$$

Here, the acoustic phonon is treated, as is normal, as quasielastic in that the energy transferred to the acoustic mode is considerably smaller than the carrier energy,[39,40] and the delta function in (9) serves to conserve the energy in the process. The overlap integral gives the mode-to-mode coupling as

$$I_{i,j}^{i',j'} = \frac{A}{4\pi^2 V}\int\int dydz[\varphi_{i,j}^*(y,z)\varphi_{i',j'}(y,z)]^2, \tag{10}$$

where $\varphi_{i,j}(y,z)$ is the transverse wave function in the particular slice. The difference here from the form in a quantum well is that these transverse wave functions are two dimensional rather than one dimensional, while the momentum vector k is a one-dimensional quantity.

In the above equations, E_k and $E_{k'}$ are the energies corresponding to the initial and final energy states in the assumed parabolic subbands, which may be defined through the use of Fig. 1. Here, we illustrate a simple two subband model to define the initial and final energies. $E_{0,ij}$ is the energy value corresponding to $k_x=0$ in the initial subband, while $E_{0,i'j'}$ corresponds to the value of the energy in the final subband with a $k_x'=0$ value. With these definitions,

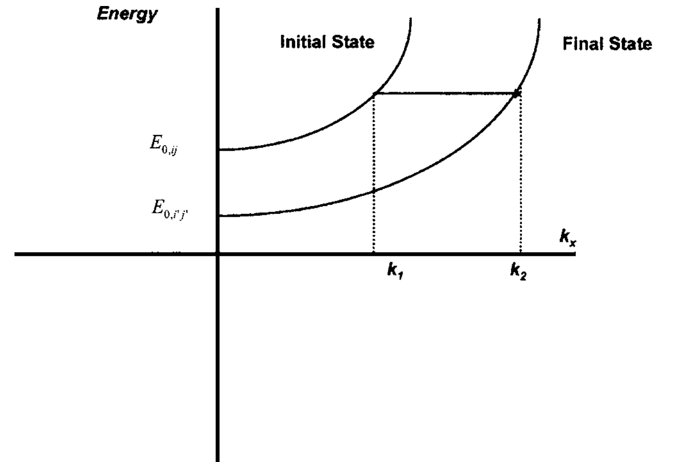

FIG. 1. Schematic of the parabolic band structure used in the formulation of the scattering method.

$$E_k = E_{0,ij} + \frac{\hbar^2 k_1^2}{2m_x^*} \tag{11}$$

and

$$E_{k'} = E_{0,i'j'} + \frac{\hbar^2 k_2^2}{2m_x^*}. \tag{12}$$

From this, the difference between the initial and final energies becomes

$$E_k - E_{k'} = E_{0,ij} - E_{0,i'j'} + \frac{\hbar^2}{2m_x^*}(k_1^2 - k_2^2). \tag{13}$$

To solve for k_2 in terms of k_1 and the difference between the initial and final energies, we denote

$$\Delta_{ij}^{i'j'} = E_{0,ij} - E_{0,i'j'} \tag{14}$$

and

$$k_2^2 = k_1^2 + \frac{2m_x^*}{\hbar^2}\Delta_{ij}^{i'j'}. \tag{15}$$

Following the usual procedure, the summation over final momentum states is replaced with an integration as

$$\sum_{k'} \to \frac{L}{2\pi}\int_{-\infty}^{\infty} dk' = \int_0^{\infty} \rho_{1\mathrm{D}}(E')dE'. \tag{16}$$

We now combine (16) with (10) to obtain

$$\left(\frac{1}{\tau_{\mathrm{ac}}}\right)_{i,j}^{i',j'} = \frac{\pi D_{\mathrm{ac}}^2 k_B T}{\hbar\rho v_s^2} I_{i,j}^{i',j'} \frac{L}{2\pi}\frac{1}{|\partial E_{k'}/\partial k'|}, \tag{17}$$

where the last term is evaluated using (15). The scattering rate is then

Downloaded 09 Jul 2010 to 128.174.190.86. Redistribution subject to AIP license or copyright; see http://jap.aip.org/jap/copyright.jsp

$$\left(\frac{1}{\tau_{\rm ac}}\right)_{i,j}^{i',j'} = \frac{m_x^* D_{\rm ac}^2 k_B T}{2\hbar^3 \rho v_s^2} \frac{L I_{i,j}^{i',j'}}{\sqrt{k^2 + (2m_x^* \Delta_{ij}^{i'j'}/\hbar^2)}} \times \theta\left(k^2 + \frac{2m_x^* \Delta_{ij}^{i'j'}}{\hbar^2}\right), \quad (18)$$

where θ is the Heaviside step function [$\theta(x)=1$ for $x>0$, and 0 for $x<0$].

Now, for our real-space quantum transport approach, we need to reverse the Fourier transform in (7). That is, we use the inverse transform to real space from momentum space and obtain the final form for the acoustic deformation potential scattering rate. The Fourier integral is

$$\left(\frac{1}{\tau}\right)_{i,j}^{i',j'}(x-x') = \frac{m_x^* D_{\rm ac}^2 k_B T}{2\hbar^3 \rho v_s^2} (L I_{i,j}^{i',j'}) \frac{1}{\sqrt{2\pi}} \times \int_{\beta}^{\infty} \frac{e^{ik(x-x')}}{\sqrt{k^2 + (2m_x^* \Delta_{ij}^{i'j'}/\hbar^2)}} dk,$$

$$\beta = \sqrt{-\frac{2m_x^* \Delta_{ij}^{i'j'}}{\hbar^2}}. \quad (19)$$

The lower limit in the integration results in zero if $\Delta_{ij}^{i'j'}>0$. From Fig. 1, it can be seen that scattering cannot occur from the lower subband to the upper subband unless there is a minimum momentum (or energy), and this accounts for the nonzero lower limit in the integration for such situations. We consider the case of $\Delta_{ij}^{i'j'} \leqslant 0$ here, and the integration can then be carried out easily to yield (the other cases are also easily done)

$$\left(\frac{1}{\tau}\right)_{i,j}^{i',j'}(x-x') = \frac{m_x^* D_{\rm ac}^2 k_B T}{2\hbar^3 \rho v_s^2} (L I_{i,j}^{i',j'}) \frac{1}{\sqrt{2\pi}} \left\{ \frac{\pi}{2} - \beta Si \times [-i\beta(x-x')] \cosh[\beta(x-x')] - \beta Ci \times [-i\beta(x-x')] \sinh[\beta(x-x')] \right\}. \quad (20)$$

The term in curly brackets is sharply peaked around $x=x'$, which implies the scattering is local with regard to the individual slices in the recursion. There is coupling between the modes within a slice, but this local (to the slice) behavior is just the normal assumption in quasiclassical cases, where the scattering is assumed to be local in space.[41] Yet we need to know the total scattering rate within the slice, so this is achieved by integrating over x' in order to find the resultant scattering weight

$$\left(\frac{1}{\tau_{\rm ac}}\right)_{i,j}^{i',j'} = \frac{m_x^* D_{\rm ac}^2 k_B T}{4\hbar^3 \rho v_s^2} (L I_{i,j}^{i',j'}) \sqrt{\frac{\pi}{2}}. \quad (21)$$

Finally, this scattering rate must be converted to the site representation with a unitary transformation

$$\Gamma_{\rm ac} = {\rm Im}\{\Sigma\} = U^+ \left(\frac{\hbar}{\tau_{\rm ac}}\right)_{i,j}^{i',j'} U, \quad (22)$$

where U is a unitary mode-to-site transformation matrix. The unitary matrix U^+ results from the eigenvalue solutions in the transverse slice and are composed of the various eigenfunctions in the site basis. Hence, it represents a mode-to-slice transformation.

B. Optical phonons

Scattering between the equivalent valleys of silicon is carried out by high-energy optical modes. In general, there two types of phonons, the f phonons between valleys on different axes in momentum space and g phonons between the two valleys along the same coordinate axis.[42,43] There are several phonons which can contribute to each of these processes,[44] but the treatment for each is the same. The differences from the acoustic mode treatment lie in the fact that the energy of the phonon can no longer be ignored in (13), and the phonon distribution function cannot be approximated by a equipartition approximation. Hence, we need to treat the emission and absorption of phonons differently, but the result is very similar. In general, the case for phonon absorption yields the result [analogous to (18)]

$$\left(\frac{1}{\tau_{iv\text{-ab}}}\right)_{i,j}^{i',j'} = \frac{m_x^* D_{iv}^2 N_q}{8\pi^2 \rho \hbar^2 \omega_q L} (I_{i,j}^{i',j'}) \frac{1}{\sqrt{k^2 + (2m_x^* \Delta_{i,j}^{i',j'}/\hbar^2)}} \times \theta\left(k^2 + \frac{2m_x^* \Delta_{i,j}^{i',j'}}{\hbar^2}\right), \quad (23)$$

where now

$$\Delta_{ij}^{i'j'} = E_{0,ij} - E_{0,i'j'} + \hbar\omega_q. \quad (24)$$

In the case of the emission of a phonon, N_q in (23) is replaced by N_q+1, and the positive sign in front of the phonon energy in (24) is replaced by a negative sign. However, there are further complications in the case of phonon emission which we will address below. For the absorption case, it is apparent that the form of the resulting equation is the same as that of the acoustic phonons, and we can use the same integration results for the inverse Fourier transform and for the site summation to yield the scattering strength. Basically, only the parameters in the leading coefficient are changed. Hence, we can immediately adapt (21) to give the result

$$\left(\frac{1}{\tau_{iv\text{-ab}}}\right)_{i,j}^{i',j'} = \frac{m_x^* D_{iv}^2 N_q}{8\pi^2 \rho \hbar^2 \omega_q L} (I_{i,j}^{i',j'}) \sqrt{\frac{\pi}{2}}. \quad (25)$$

Once again, this is now inserted into (22) to get the site representation.

As mentioned above, the emission case has some complications. We must consider three different cases corresponding to different values for the energy difference from the initial subband to the final subband and the emitted phonon energy: $\Delta_{ij}^{i'j'}<0$, $\Delta_{ij}^{i'j'}>0$, and $\Delta_{ij}^{i'j'}=0$. In each case, the Fourier transform is solved through the use of contour integrations.

Downloaded 09 Jul 2010 to 128.174.190.86. Redistribution subject to AIP license or copyright; see http://jap.aip.org/jap/copyright.jsp

(1) $\Delta_{ij}^{i'j'} < 0$

The resultant Fourier integral is

$$\left(\frac{1}{\tau}\right)_{i,j}^{i',j'}(x-x') = \frac{m_x^* D_{iv}^2 (N_q+1)}{8\hbar^2 \rho \omega_q L}(I_{i,j}^{i',j'})\frac{1}{\sqrt{2\pi}} \times \int_0^\infty \frac{\cos[k_0(x-x')]}{\sqrt{k^2-\beta^2}}dk. \tag{26}$$

While an exact closed form for the integral cannot be found, it can be closely approximated as

$$\left(\frac{1}{\tau_{iv\text{-em}}}\right)_{i,j}^{i',j'}(x-x') = \frac{m_x^* D_{iv}^2 (N_q+1)}{8\pi^2 \rho \hbar^2 \omega_q L}(I_{i,j}^{i',j'}) \times \left[-\frac{\pi}{2}N_0(x-x')\right]. \tag{27}$$

As previously, this is localized, and we integrate over x' to get the total scattering strength. This leads to

$$\left(\frac{1}{\tau_{iv\text{-em}}}\right)_{i,j}^{i',j'} = \frac{m_x^* D_{iv}^2 (N_q+1)}{8\pi^2 \rho \hbar^2 \omega_q L}(I_{i,j}^{i',j'}). \tag{28}$$

(2) $\Delta_{ij}^{i'j'} > 0$

The major factor here is the change in the sign of the second term in the square root in the denominator of (26), which leads to

$$\left(\frac{1}{\tau}\right)_{i,j}^{i',j'}(x-x') = \frac{m_x^* D_{iv}^2 (N_q+1)}{8\hbar^2 \rho \omega_q L}(I_{i,j}^{i',j'})\frac{1}{\sqrt{2\pi}} \times \int_0^\infty \frac{\cos[k_0(x-x')]}{\sqrt{k^2+\beta^2}}dk = \frac{m_x^* D_{iv}^2 (N_q+1)}{8\hbar^2 \rho \omega_q L}(I_{i,j}^{i',j'})\frac{1}{\sqrt{2\pi}}K_0(x-x'). \tag{29}$$

Using an asymptotic expansion of the Bessel function of an imaginary argument results in

$$\left(\frac{1}{\tau}\right)_{i,j}^{i',j'}(x-x') = \frac{m_x^* D_{iv}^2 (N_q+1)}{8\hbar^2 \rho \omega_q L}(I_{i,j}^{i',j'})\frac{1}{\sqrt{2\pi}} \times \sqrt{\frac{\pi}{2(x-x')}}e^{-(x-x')}. \tag{30}$$

We now integrate x' to determine the total scattering strength. The final result is

$$\left(\frac{1}{\tau_{iv\text{-em}}}\right)_{i,j}^{i',j'}(x-x') = \frac{m_x^* D_{iv}^2 (N_q+1)}{16\pi \rho \hbar^2 \omega_q L}(I_{i,j}^{i',j'})\Gamma\left(\frac{3}{2}\right). \tag{31}$$

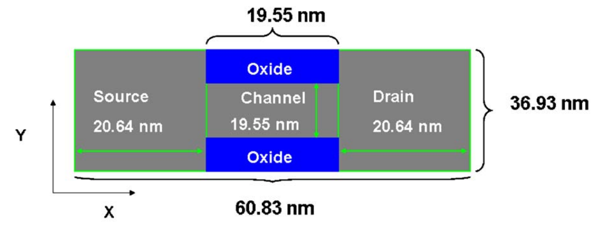

FIG. 2. (Color online) Schematic of the device design in the *xy* plane. Due the size of the device considered here, we are constrained only by acoustic deformation potential scattering, intervalley scattering, and electron-impurity interactions. These constraints make this device ideal for confirming the model by measuring the electron mobility.

(3) $\Delta_{ij}^{i'j'} = 0$

In this case, the Fourier integral is

$$\left(\frac{1}{\tau}\right)_{i,j}^{i',j'}(x-x') = \frac{m_x^* D_{iv}^2 (N_q+1)}{8\hbar^2 \rho \omega_q L}(I_{i,j}^{i',j'})\frac{1}{\sqrt{2\pi}} \times \int_0^\infty \frac{\cos[k_0(x-x')]}{k}dk = \frac{m_x^* D_{iv}^2 (N_q+1)}{8\hbar^2 \rho \omega_q L}(I_{i,j}^{i',j'})\frac{1}{\sqrt{2\pi}} \times [-Ci(x-x')]. \tag{32}$$

Once again, x' is integrated out of the equation to determine the magnitude of the delta function. The final result is

$$\left(\frac{1}{\tau_{iv\text{-em}}}\right)_{n'm'}^{nm} = \frac{m_x^* D_{iv}^2 (N_q+1)}{8\sqrt{2}\pi^{5/2} \rho \hbar^2 \omega_q L}(I_{n'm'}^{nm}). \tag{33}$$

C. Bulk mobility

In order to check that the self-energy expressions developed here yield the correct results, we compute the mobility of a "large" sample of silicon and compare our results with those previously published.[45–47] The structure of this device is shown in Fig. 2. The thickness of the silicon layer is 16.29 nm, the width of the channel is 16.29 nm, and the length of the channel is 19.55 nm (here the dimensions are set by integer multiples of the silicon lattice constant for reasons discussed below). Oxide barriers have been placed on either side of the channel to simulate the appearance of a hard wall boundary that would be present in an actual experimental system. The source and drain of the device are 36.93 nm wide and 20.67 nm in length. The exact dimensions are used to aid in the inclusion of dopants, which are put on the lattice sites.[13] The silicon lattice is traversed and dopants are placed in the various regions if a generated random number is less than the ratio between the nominal doping of the region and the volume of silicon atoms in the region. The charge associated with the dopant atoms is then mapped back to the mesh and included in the self-consistent Poisson solution for the potential. Exchange and correlations terms are included through a local density approximation.[33] The source and drain of the device are doped n-type with a doping concentration of 1×10^{20} cm^{-3}, while the n-type channel doping concentration is varied. In a structure of this

Downloaded 09 Jul 2010 to 128.174.190.86. Redistribution subject to AIP license or copyright; see http://jap.aip.org/jap/copyright.jsp

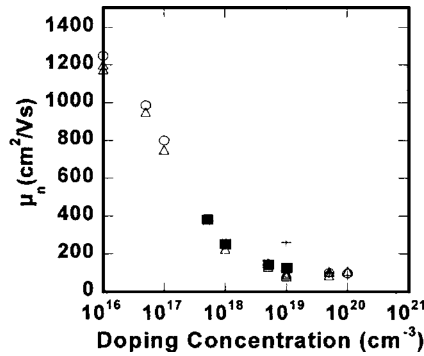

FIG. 3. Plot of the calculated (square) and the measured mobility data from Sze and Irvin [104] (circle), Mousty *et al.* [105] (triangle) and from Logan *et al.* [106] (cross)vs the channel doping density.

size, the main types of scattering are acoustic deformation potential, equivalent intervalley, and impurity scattering. Because the impurities are treated in real space with their actual Coulomb potential, we do not need the self-energy terms for them.

We now use the quantum transport simulation to determine the resistance of the device and determine the mobility, since we know the doping concentration in the channel. In Fig. 3, we plot the electron mobility at 300 K as a function of the channel doping density and the experimental data from Refs. 46–48 is included for comparison. At this point, it is crucial to mention how vital self-consistency is when making these types of calculations. Without the self-consistency, the electrons would not correctly interact with the dopants in the system. This would cause the calculated mobility to differ from the experimental values by as much as an order of magnitude, since one of the main mobility limiting interactions in grossly underestimated. When we compare these with the experimental measurements, we find that at the lowest doping density, there is almost no difference between the measured mobility and our calculated mobility. As the doping density is increased, we find that the calculated mobility differs from the actual mobility by less than 1%. This difference includes the fact that small grid modifications were made to account for the increased energies of the carriers in more heavily doped systems. Since changes in the grid spacing induce changes in the artificial band structure of the system,[13] some small differences between the experimental and calculated mobility are inevitable. However, the size of the discrepancy is such that none of the relevant transport parameters would be affected by a discrepancy of this type, and the results are certainly less than the error in the experiment or in this theory. Further, we find that the current conservation with this scattering model is similar to that in the ballistic case. We conclude that the current conservation here is limited by the meshing of the solution space rather than by the inclusion of a nonphysical process which is artificially removing electrons from the system.

One concern is whether the structure used is sufficiently large to be termed "bulk." We have performed simulations for a larger structure for selected doping levels, with no change found in the mobility. Hence, we conclude that our ~20 nm size is effectively bulk in silicon.

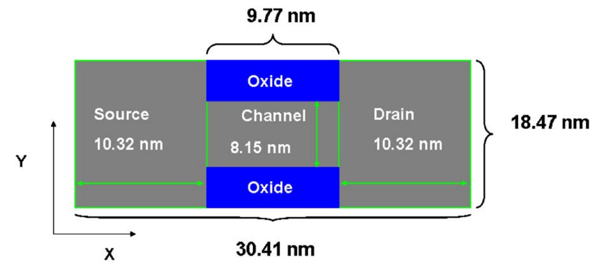

FIG. 4. (Color online) Schematic of the quantum-wire device design in the *xy* plane.

III. BALLISTIC TO DIFFUSIVE CROSSOVER

We now turn our attention to the quantum-wire transistors of interest. We examine a system where the quantum-mechanical nature of the scattering matrices is needed to correctly characterize the system. In a system such as this, the phonon scattering should have a more profound effect on the transport, as the reduced area of the wire should give rise to an enhanced overlap integral in the scattering calculations. We consider the system shown in Fig. 4. The thickness of the silicon layer has now been reduced to 6.51 nm and the width of the channel is 8.15 nm. The length of the quantum wire that comprises the channel will be varied to study the resistance of the channel. Oxide barriers are placed on either side of the channel to simulate the appearance of a hard wall boundary that would be present in an actual experimental system. The source and drain of the device are 18.47 nm wide and 10.32 nm in length. The latter is discretely doped n-type with a doping concentration of 1×10^{20} cm^{-3}, while the channel is undoped. The quantum wire that forms the channel of the device has metal gates on three sides to form a trigate-type transistor.[48] The gate oxide thickness (SiO_2) on this device is 1 nm. As previously, this simulation is carried out at 300 K.

In general, it has been suggested that the transport in small transistors is ballistic, and that once a carrier enters the channel it will continue to the drain, with no chance to scatter back to the source.[10,12] Already, however, Svizhenko and Anantram have shown that scattering within the channel will cause second-order effects which do affect the terminal characteristics of the transistor.[49] The search for ballistic behavior has not been so successful, and one has had to estimate the degree to which ballistic transport appears in the device. Here, we want to vary the length of the channel in our nanowire transistor to determine when the ballistic transport converts to diffusive transport (mobility-dominated transport). When the transport is ballistic the resistance of the channel will be determined by the inverse of the Landauer conductance as

$$R_{\text{ballistic}} = \left[\frac{2e^2}{h}N\right]^{-1}, \tag{34}$$

where N is the number of transverse modes propagating through the wire. Importantly, there is no dependence upon the length of the wire. On the other hand, when the resistance is determined by the mobility and carrier density, then the resistance is given by

Downloaded 09 Jul 2010 to 128.174.190.86. Redistribution subject to AIP license or copyright; see http://jap.aip.org/jap/copyright.jsp

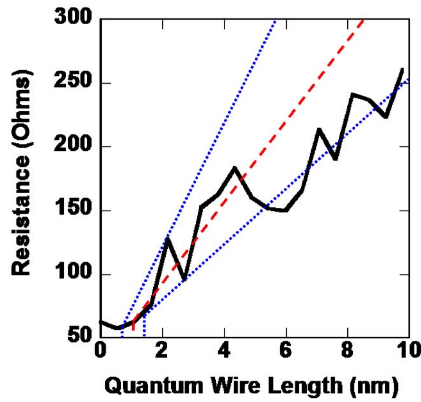

FIG. 5. (Color online) Resistance of a silicon quantum-wire nanotransistor as the length of the quantum wire in the channel is varied with V_g=0.5 V and V_d=10 mV. After the initial ballistic region, we see the expected linear increase in the resistance as the channel length is increased. The blue lines show the maximum and minimum values of the ballistic-diffusive crossover length and the red line shows the median value taken when the length is calculated through the center of the data.

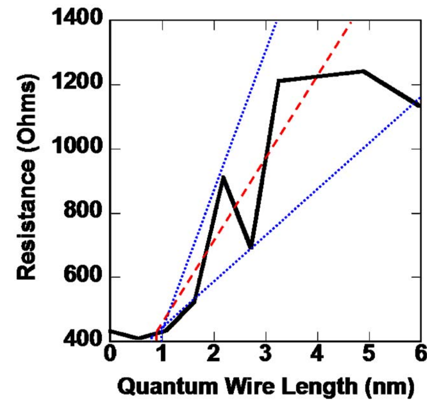

FIG. 6. (Color online) Resistance of a silicon quantum-wire nanotransistor as the length of the quantum wire in the channel is varied with V_g=0.5 V and V_d=100 mV. Once again, we find that the resistance increases linearly after the initial ballistic region. The blue lines show the maximum and minimum values of the ballistic-diffusive crossover length and the red line shows the median value taken when the length is calculated through the center of the data.

$$R_{\text{diffusive}} = \left[\frac{1}{\sigma}\right]\frac{L}{A} = \frac{1}{ne\mu}\frac{L}{A}, \tag{35}$$

where L is the channel length and A is the "cross-sectional area" of the inversion layer. We use the area here, rather than just the width of the two-dimensional layer, as we are dealing with a three-dimensional wire with full quantization in the transverse direction. Clearly, in this latter case, the resistance increases linearly with the channel length. It is the change from (34) and (35) that we seek in the present study.

In Fig. 5, we plot the resistance of our silicon nanowire transistor with the gate and drain voltages of the device held constant at V_g=0.5 V and V_d=10 mV, respectively. The gate voltage is sufficiently high that we are guaranteed to have an inversion layer formed in the channel of the device. One may wonder why we do not use a higher drain voltage, but we must operate in the linear region of the device. At higher drain voltages, one begins to get depletion at the drain end, and (35) is no longer valid. In the figure, the resistance of the quantum wire is initially fairly constant when the length of the wire is held to less than 2 nm. When the length of the wire then exceeds *roughly* 2 nm, we find that the resistance of the device begins to increase linearly as is characteristic for devices in the diffusive transport regime. However, there are oscillations which appear. These can be found not only in the conductance and output current of the quantum wire, but in the density as well. These oscillations arise from the strong quantum interference between the source and drain ends of the device. This oscillatory result of the quantum interference is generally seen in the conductance both experimentally[50] and theoretically.[51,52] Nevertheless, we can estimate the crossover by seeking the crossing point of a line down the center of the linearly increasing part and a line horizontal in the center of the ballistic curve, as shown in the figure (dashed curve). The range of possible values is set by the dotted limiting curves. Projection of these crossings onto the horizontal axis gives us the appropriate dimensions. From this plot, we estimate the ballistic to diffusive crossover occurs at 1.42±0.03 nm.

In Fig. 6, we show a similar plot for the case in which the drain voltage has been increased to V_d=100 mV. The same general trends appear here as in Fig. 5. We find a region in which the transport is ballistic indicated by virtually no change in the current as the wire is lengthened. This is once again followed by the typically expected linear region. The ballistic to diffusive crossover is much shorter than in Fig. 5, and occurs at 0.87±0.10 nm. This is due to the fact that, in this case, the carriers are accelerated, and heated, to the point that the phonon interaction is stronger in the drain than in the source, and therefore, accounts for the majority of the increase in channel resistance. In the case of Fig. 6 though, we find that the resistance of the quantum wire is dramatically increased as compared to that of Fig. 5, which we attribute to considerable carrier heating (100 mV across 10 nm corresponds to 100 kV/cm, which is well into the hot-electron region in silicon).

The reduction of the ballistic to diffusive crossover is summarized in Fig. 7, where we plot the crossover length for three different drain voltages. There is a clear linear trend, within the error associated with the measurements, in the reduction of the ballistic to diffusive crossover by the en-

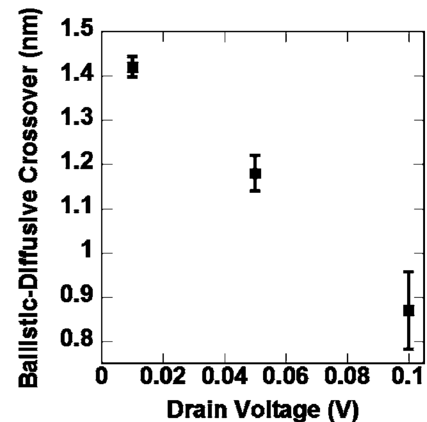

FIG. 7. Ballistic to diffusive crossover length for three different drain voltages.

Downloaded 09 Jul 2010 to 128.174.190.86. Redistribution subject to AIP license or copyright; see http://jap.aip.org/jap/copyright.jsp

hanced phonon scattering in the drain of the silicon nanowire transistor. The more energy the carriers gain as they traverse the length of the nanowire transistor, the more scattering they see. Thus there is a linear drop in the ballistic to diffusive crossover length with increases in drain voltage, as discussed above.

IV. CONCLUSIONS

In this paper, we have presented a simple physical approach to including separable scattering mechanisms as a self-energy in a real-space quantum simulation for a nanowire transistor. The inclusion of separable phonon-scattering mechanism is crucial in understanding the role that phonon processes play in electrical transport in quantum confined systems. We derived the scattering contributions for acoustic deformation potential and intervalley phonon scattering with both *f*- and *g*-type processes included, and verified that our model captures the experimentally verified mobility for silicon. When the model is applied to a gated quantum-wire structure, we find the largest ballistic to diffusive crossover length in the device occurs with the smallest bias. We find this length to be about 1.4 nm. Increasing the drain bias decreases this ballistic to diffusive crossover length, presumably due to considerable carrier heating in the channel. These results demonstrate that the limit for ballistic device performance is much less than previously thought.

ACKNOWLEDGMENTS

This work is supported by the Office of Naval Research and by Intel Corporation.

[1]G. E. Moore, Electronics **38**, 114 (1965).
[2]See, e.g., R. Chau *et al.*, IEEE Trans. Nanotechnol. **4**, 153 (2005).
[3]J. Kedzierski, J. Bokor, and E. Anderson, J. Vac. Sci. Technol. B **17**, 3244 (1999).
[4]B. Doris *et al.*, Tech. Dig. - Int. Electron Devices Meet. **2001**, 937.
[5]B. Yu *et al.*, Tech. Dig. - Int. Electron Devices Meet. **2002**, 267.
[6]J. R. Barker and D. K. Ferry, Solid-State Electron. **23**, 531 (1980).
[7]M. Fischetti, J. Appl. Phys. **83**, 270 (1998).
[8]K. Likharev, in *Advanced Semiconductor and Organic Nano-Techniques*, edited by H. Morkoc (Academic, New York, 2002).
[9]R. Venugopal *et al.*, J. Appl. Phys. **92**, 3730 (2002).
[10]K. Natori, J. Appl. Phys. **76**, 4879 (1994).
[11]M. J. Gilbert *et al.*, J. Comput. Electron. **2**, 329 (2003).
[12]M. Lundstrom, IEEE Electron Device Lett. **18**, 361 (1997).
[13]M. J. Gilbert and D. K. Ferry, J. Appl. Phys. **95**, 7954 (2004).
[14]H. Benisty, Phys. Rev. B **51**, 13281 (1995).
[15]M. G. Pala and G. Iannaccone, Phys. Rev. Lett. **93**, 256803 (2004).
[16]G. Neofotistos, R. Lake, and S. Datta, Phys. Rev. B **43**, 2442 (1991).
[17]R. Akis, J. P. Bird, and D. K. Ferry, J. Phys.: Condens. Matter **8**, L667 (1996).
[18]W. R. Frensley, Rev. Mod. Phys. **62**, 745 (1990).
[19]R. Gebauer and R. Car, Phys. Rev. B **70**, 125324 (2004).
[20]M. Büttiker, Phys. Rev. Lett. **57**, 1761 (1986).
[21]R. Venugopal *et al.*, J. Appl. Phys. **93**, 5613 (2003).
[22]H. Dekker, Phys. Rev. A **16**, 2126 (1977).
[23]H. L. Grubin *et al.*, Semicond. Sci. Technol. **9**, 855 (1994).
[24]N. C. Kluksdahl *et al.*, Phys. Rev. B **39**, 7720 (1989).
[25]T. Usuki *et al.*, Phys. Rev. B **52**, 8244 (1995).
[26]D. S. Fisher and P. A. Lee, Phys. Rev. B **23**, 6851 (1981).
[27]D. K. Ferry and S. M. Goodnick, *Transport in Nanostructures* (Cambridge University Press, Cambridge, 1997).
[28]R. Kotlyar *et al.*, Appl. Phys. Lett. **84**, 5270 (2004).
[29]E. G. Emberly and G. Kirczenow, Phys. Rev. B **61**, 5740 (2000).
[30]R. Lake and S. Datta, Phys. Rev. B **45**, 6670 (1992).
[31]L. F. Register and K. Hess, Phys. Rev. B **49**, 1900 (1994).
[32]A. L. Fetter and J. D. Walecka, *Quantum Theory of Many-Particle Systems* (McGraw-Hill, New York, 1971).
[33]Y. Wang, J. Wang, H. Guo, and E. Zaremba, Phys. Rev. B **52**, 2738 (1995).
[34]L. P. Kadanoff and G. Baym, *Quantum Statistical Mechanics* (Benjamin/Cummings, Reading, MA, 1962).
[35]J. Rammer, *Quantum Transport Theory* (Perseus, Reading, MA, 1998).
[36]See, e.g., R. Lake *et al.*, J. Appl. Phys. **81**, 7845 (1997).
[37]V. Špička, B. Velický, and A. Kalvová, Physica E (in press).
[38]T. Ando, A. Fowler, and F. Stern, Rev. Mod. Phys. **54**, 437 (1982).
[39]H. Brooks, Adv. Phys. **7**, 85 (1955).
[40]W. Schockley, *Electrons and Holes in Semiconductors* (Van Nostrand, Princeton, NJ, 1950).
[41]J. R. Barker, in *Physics of Nonlinear Transport in Semiconductors*, edited by D. K. Ferry, J. R. Barker, and C. Jacoboni (Plenum, New York, 1980), p. 126.
[42]D. Long, Phys. Rev. **120**, 2024 (1960).
[43]D. K. Ferry, Phys. Rev. B **12**, 2361 (1975).
[44]See, e.g., D. K. Ferry, *Semiconductors* (Macmillan, New York, 1991).
[45]S. M. Sze and J. C. Irvin, Solid-State Electron. **11**, 599 (1968).
[46]F. Mousty, P. Ostoja, and L. Passari, J. Appl. Phys. **45**, 4576 (1974).
[47]R. A. Logan, J. F. Gilbert, and F. A. Trumore, J. Appl. Phys. **32**, 131 (1961).
[48]H. S. Doyle *et al.*, IEEE Electron Device Lett. **24**, 263 (2003).
[49]A. Svizhenko and M. P. Anantram, IEEE Trans. Electron Devices **50**, 1459 (2003).
[50]A. T. Tilke *et al.*, Phys. Rev. B **68**, 075311 (2003).
[51]V. A. Sablikov, S. V. Polyakov, and M. Buttiker, Phys. Rev. B **61**, 13763 (2000).
[52]G. Kirczenow, Phys. Rev. B **39**, 10452 (1989).

Downloaded 09 Jul 2010 to 128.174.190.86. Redistribution subject to AIP license or copyright; see http://jap.aip.org/jap/copyright.jsp